

Origins of phase contrast in the atomic force microscope in liquids

John Melcher^a, Carolina Carrasco^{b,c}, Xin Xu^a, José L. Carrascosa^d, Julio Gómez-Herrero^b, Pedro José de Pablo^b, and Arvind Raman^{a,1}

^aSchool of Mechanical Engineering and Birk Nanotechnology Center, Purdue University, West Lafayette, IN 47907; ^bDepartamento de Física de la Materia Condensada C-III, Universidad Autónoma de Madrid, 28049 Madrid, Spain; ^cInstituto de Ciencia de Materiales de Madrid, Centro Nacional de Biotecnología, Consejo Superior de Investigaciones Científicas, 28049 Madrid, Spain; and ^dDepartamento de Estructura de Macromoléculas, Centro Nacional de Biotecnología, Consejo Superior de Investigaciones Científicas, 28049 Madrid, Spain

Edited by Jean-Pierre Aime, Centre de Physique Moleculaire Optique et Hertzienne, Bordeaux, France and accepted by the Editorial Board June 19, 2009 (received for review March 2, 2009)

We study the physical origins of phase contrast in dynamic atomic force microscopy (dAFM) in liquids where low-stiffness microcantilever probes are often used for nanoscale imaging of soft biological samples with gentle forces. Under these conditions, we show that the phase contrast derives primarily from a unique energy flow channel that opens up in liquids due to the momentary excitation of higher eigenmodes. Contrary to the common assumption, phase-contrast images in liquids using soft microcantilevers are often maps of short-range conservative interactions, such as local elastic response, rather than tip-sample dissipation. The theory is used to demonstrate variations in local elasticity of purple membrane and bacteriophage ϕ 29 virions in buffer solutions using the phase-contrast images.

atomic force microscopy | liquid environments | energy dissipation | higher eigenmodes | momentary excitation

Dynamic atomic force microscopy (dAFM) is an essential experimental tool for the study of conservative and dissipative forces on surfaces at nanometer length scales, which has major implications for the physics of biomolecular interactions, chemical bond kinetics, adhesion, wetting and capillary action, friction and elasticity on material surfaces (1, 2). dAFM techniques have been developed to distinguish between dissipative (friction, viscoelastic, bond breaking, surface hysteresis, capillary condensation) and conservative (elastic, magnetic, electrostatic) forces between a sharp oscillating tip and the surface. In amplitude-modulated AFM (AM-AFM) phase-contrast imaging, the variation in the phase of the oscillating probe tip with respect to the drive signal is mapped over the sample. For the past decade phase contrast has been intimately connected with variation in tip-sample dissipation over the sample (2–6). Phase-contrast imaging is widely recognized as perhaps the most important AM-AFM mode for the measurement of compositional contrast.

The connection between phase contrast and tip-sample dissipation rests on the assumption that the cantilever dynamics can be modeled by a single eigenmode (point-mass) oscillator. With this assumption, the tip-sample dissipation can be equated to the difference between work input to the oscillator and energy dissipated into a surrounding viscous medium (4, 5). This theory forms the bedrock upon which phase-contrast imaging is currently based, at least under ambient and vacuum conditions.

dAFM is now a well-known and broadly extended technique for nanoscale imaging and force spectroscopy in the biology community (7–10). Because the natural medium for the study of biological samples is liquid, it is of fundamental importance to develop a proper description of the different working modes of dAFM when the probe and sample are immersed in liquids. In particular, there is little work on understanding the origins of phase contrast in liquids (6) where soft cantilevers (stiffness $\lesssim 1$ N/m) with low-quality factors ($Q \lesssim 5$) are routinely used for the imaging of soft biological samples. It is important to note that all prior theoretical works on phase contrast, both in air and liquids, are based on the

assumption that a single eigenmode is sufficient to describe the microcantilever dynamics (2).

In this article, we build on a recent result (11)—valid for soft microcantilevers tapping on a sample in liquids—that shows the second eigenmode is momentarily excited near times of tip-sample contact. This finding implies that the dynamics of soft microcantilevers in liquids is naturally multimodal. We show that this opens up a new energy flow channel for the soft microcantilevers in liquids and that phase contrast really measures the extent of energy transferred to the second eigenmode via tip-sample interaction rather than tip-sample dissipation. We demonstrate that in situations where electrostatic bilayer forces and tip-sample adhesion are negligible, phase contrast becomes a mapping of local elastic stiffness variations of the sample. Experimental phase-contrast images on purple membrane and ϕ 29 viral capsids in buffer solution are used to verify the theoretical findings by linking these images with the local variations of the sample stiffness.

Theoretical Considerations

Mathematical Modeling. We begin with a general mathematical model governing the dynamics of a soft cantilever tapping on a sample in liquid, for which at least a 2-eigenmode model is required (11):

$$\frac{\ddot{q}_1}{\omega_1^2} + \frac{\dot{q}_1}{\omega_1 Q_1} + q_1 = \frac{F_1}{k_1} \cos(\omega t) + \frac{F_{ts}(d, \dot{d}, m)}{k_1} \quad [1a]$$

$$\frac{\ddot{q}_2}{\omega_2^2} + \frac{\dot{q}_2}{\omega_2 Q_2} + q_2 = \frac{F_2}{k_2} \cos(\omega t) + \frac{F_{ts}(d, \dot{d}, m)}{k_2} \quad [1b]$$

where q_i is the contribution to tip deflection of the i^{th} eigenmode and dots represent temporal derivatives. F_i , k_i , Q_i , and ω_i ($i = 1, 2$) refer to the equivalent forcing amplitudes and stiffnesses (12), quality factors, and natural frequencies of the first 2 eigenmodes respectively. ω is the drive frequency and $T = 2\pi/\omega$ is the excitation time period. Moreover, $\omega \approx \omega_1$ for the conventional tapping-mode imaging where the drive frequency is tuned to the natural frequency of the first eigenmode. $F_{ts}(d, \dot{d}, m)$ is the nonlinear tip-sample interaction force, where $d = Z + q_1 + q_2$ is the instantaneous tip-sample gap for a base-sample separation Z and m is a Boolean variable indicating the state of the tip-sample contact in the case of hysteretic force models; i.e. $m = 1$ for contact and $m = 0$ otherwise (13, 14). For steady-state oscillations, let A_1 and ϕ_1 refer to the amplitude and phase lag, respectively,

Author contributions: J.M., J.G.-H., P.J.d.P., and A.R. designed research; J.M., C.C., and X.X. performed research; J.M., C.C., J.L.C., J.G.-H., P.J.d.P., and A.R. analyzed data; J.L.C. contributed new reagents/analytic tools; and J.M. and A.R. wrote the paper.

The authors declare no conflict of interest.

This article is a PNAS Direct Submission. J.-P.A. is a guest editor invited by the Editorial Board.

¹To whom correspondence should be addressed. E-mail: raman@ecn.purdue.edu.

of the first harmonic of the first eigenmode response given by $A_1 \cos(\omega t - \phi_1)$. Far from the sample ($F_{ts} = 0$), A_1 tends to the unconstrained amplitude A_0 . We calculate $F_2/F_1 = -0.55$ for a uniformly distributed forcing and $k_2/k_1 = 39$ (12) from Bernoulli–Euler beam theory.

The total tip-sample interaction force $F_{ts}(d, \dot{d}, m)$ can be decomposed additively into conservative forces $F_{ts,c}(d)$ and nonconservative (dissipative) forces $F_{ts,nc}(d, \dot{d}, m)$. Conservative forces obey $F_{ts,c}(d) = -\partial V_{ts}(d)/\partial d$ for a potential function $V_{ts}(d)$ and cannot change the total mechanical energy of the probe upon completion of a periodic orbit. In liquids, the principal conservative tip-sample forces arise from elastic contact forces and the so-called DLVO (Derjaguin–Landau–Verwey–Overbeek) forces (14), which include attractive van der Waals and repulsive electrostatic double-layer forces. Hydrophobic and hydrophilic interactions can also contribute to conservative forces; however, these forces are relevant only for special tip-sample combinations. Finally, hydration layers on ordered surfaces cause oscillatory tip-sample forces (14); however, these forces are typically too small to detect with AM-AFM. Nonconservative tip-sample interaction forces of the form $F_{ts,nc}(d, \dot{d}, m)$ dissipate mechanical energy of the probe upon interaction. Nonconservative forces typically encountered in dAFM include viscoelastic forces of the form $F_{ts,nc}(d, \dot{d})$, hysteretic adhesion forces of the form $F_{ts,nc}(d, m)$, or combinations of the two (15). Common hysteretic forces in liquids include specific bond-forming/-breaking between a functionalized tip and complimentary molecule on the surface (16), or hysteretic adhesion between the tip and a highly adhesive soft surface predicted by the Johnson–Kendal–Roberts (JKR) theory (17).

Here we focus on the common scenario, where a non-functionalized tip interacts with a soft biological sample supported on a stiff substrate in a high-ionic-concentration buffer where the DLVO forces are highly screened (18, 19) and adhesion hysteresis is negligible. Accordingly, interactions between the tip and sample can be modeled by a rate-dependent (viscous) force $F_{ts,nc}(d, \dot{d})$ combined with a conservative contact force $F_{ts,c}(d)$. An example of such a model is Hertz contact (20) combined with Kelvin–Voigt viscoelastic forces (15). However, the phenomenon described here also applies for other contact theories, such as Chadwick theory for thin membranes (21) or linear contact theory for viral capsids (10). The Hertz contact model (20) is given by

$$F_{ts,c}(d) = \begin{cases} 0, & d > 0 \\ \frac{4}{3} E^* \sqrt{R} (-d)^{3/2}, & d \leq 0, \end{cases} \quad [2]$$

where $E^* = [(1 - \nu_s^2)/E_s + (1 - \nu_t^2)/E_t]^{-1}$ is the effective elastic modulus of the tip-sample combination, E_t, E_s, ν_t , and ν_s are elastic moduli and Poisson’s ratios of the tip and sample, respectively, and R is the radius of the tip. Nonconservative, viscoelastic forces (15) are modeled by

$$F_{ts,nc}(d, \dot{d}) = \begin{cases} 0, & d > 0 \\ -\eta_s \dot{d} \sqrt{R} (-d), & d \leq 0, \end{cases} \quad [3]$$

where η_s is the viscosity of the sample. In the numerical simulations presented here, all Poisson’s ratios are 0.3 and $E_t = 130$ GPa for a silicon tip with radius $R = 20$ nm.

Numerical Simulations. We begin with numerical simulations (22) of Eq. 1 for $A_0 = 10$ nm and a conventional excitation $\omega = \omega_1$ for typical cantilevers in air and liquid environments. A dissipative sample modeled by Eq. 2 and Eq. 3 with $E_s = 100$ MPa (purple membrane), $\eta_s = 10$ Pa·s is chosen for the simulations. By comparison, membrane proteins have viscosities on the order of 1 Pa·s (23). The cantilevers are excited far from the sample, where they achieve steady periodic oscillations, and are then brought

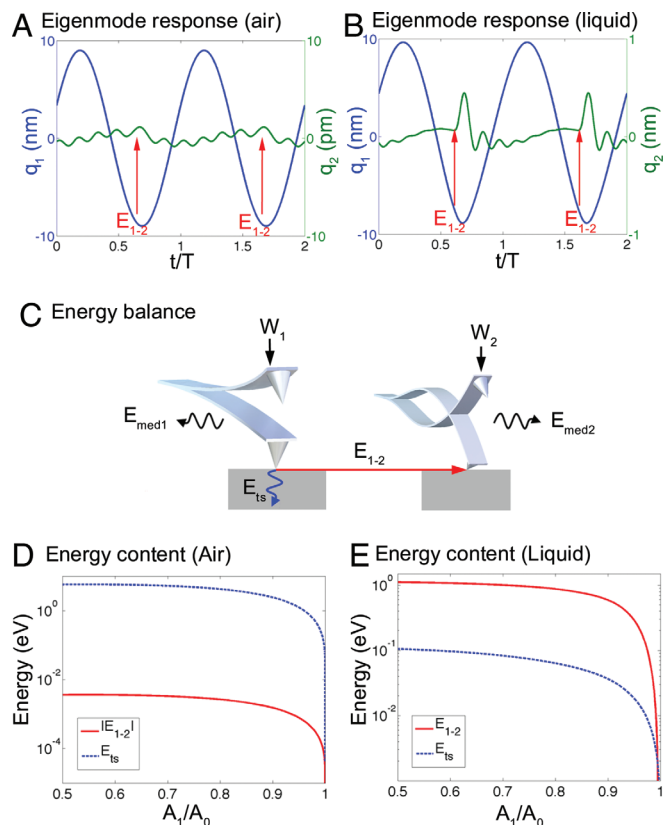


Fig. 1. Energy flow in the 2-eigenmode model. (A and B) Simulated response of the first and second eigenmode for a stiff cantilever C1 in air (A) and a soft cantilever C2 in liquid (B), both tapping on a dissipative sample ($E_s = 100$ MPa, $\eta_s = 10$ Pa·s, $A_1/A_0 = 0.9$, $A_0 = 10$ nm). In both cases, the drive frequency is tuned to the first eigenmode $\omega = \omega_1$. (C) The energy diagram for the 2-eigenmode model allows some energy E_{1-2} to flow from the first to the second eigenmode during interaction with the sample. Tip-sample dissipation E_{ts} and E_{1-2} are compared for the 2 cantilevers in air (D) and liquid (E).

close to the sample by gradually reducing Z . For the simulation in air, we consider a stiff rectangular cantilever C1 ($k_1 = 30$ N/m, $Q_1 = 400$, $Q_2 = 1200$, $\omega_1 = 2\pi \cdot 300$ kHz, $\omega_2 = 6.5\omega_1$) typical for air operation. In liquids, we choose a soft rectangular cantilever C2 ($k_1 = 0.11$ N/m, $Q_1 = 1.85$, $Q_2 = 4.3$, $\omega_1 = 2\pi \cdot 3.9$ kHz, $\omega_2 = 7.7\omega_1$) typical for liquid operation and the properties of which were measured experimentally (24). Note for both the soft and stiff microcantilevers considered here, the second eigenmode frequency is not near an integer multiple of the first, ensuring that resonant interactions between eigenmodes do not occur (25).

From these simulations, we find that the second eigenmode is significantly excited momentarily near times of contact with the sample in liquids, as compared with air, even though the drive frequency is tuned to the first eigenmode. The responses of the first and second eigenmodes are decomposed and plotted for 2 periods at an amplitude ratio of $A_1/A_0 = 0.9$ for the simulation in air (Fig. 1A) and in liquid (Fig. 1B). During interaction with the sample, some amount of energy E_{1-2} is transferred from the first to the second eigenmode. However, for the same conditions A_0 and A_1/A_0 , the momentary excitation of the second eigenmode is at least 2 orders smaller in air than in liquid. Also, because $Q_2 < \omega_2/\omega_1$ in liquid, the momentary excitation of the second eigenmode decays during the oscillation time period $T = 2\pi/\omega$, ($\omega \approx \omega_1$); i.e., the energy transfer E_{1-2} eventually dissipates into the surrounding media.

To understand the origins of phase contrast in this situation, we perform a steady-state energy flow analysis for a single

excitation period T according to the diagram in Fig. 1C. The total work performed by the excitation source is divided into W_1 and W_2 , supplied to the first and second eigenmodes, respectively. Energy can leave the first eigenmode by dissipation into the surrounding media E_{med1} , dissipation into the sample E_{ts} by nonconservative interactions or through a third energy flow channel. During interaction with the sample, the 2-eigenmode model allows energy E_{1-2} to flow from the first to the second eigenmode where it is subsequently dissipated into the surrounding media in the form of E_{med2} . The steady-state energy balance for the first eigenmode is

$$W_1 = E_{ts} + E_{1-2} + E_{med1}. \quad [4]$$

Considering an N harmonic approximation $q_1(t) \approx \sum_{n=1}^N A_n \cos(n\omega t - \phi_n)$ leads to $W_1 = \int_0^T F_1 \cos(\omega t) \dot{q}_1(t) dt = \pi F_1 A_1 \sin \phi_1$. The energy dissipated by the media is $E_{med1} = \frac{k_1}{\omega_1 Q_1} \int_0^T \dot{q}_1^2(t) dt = \frac{\pi k_1}{Q_1} \sum_{n=1}^N n^2 A_n^2$, which we define as $E_{med1} \equiv \sum_{n=1}^N E_{med1,n}$, where $E_{med1,n}$ is the energy dissipated into the surrounding media by the n^{th} harmonic of the first eigenmode. Substituting the above relations into the energy balance (Eq. 4) yields

$$\sin \phi_1 = \frac{g(\bar{\omega}_1) A_1}{A_0} \left(1 + \sum_{n=2}^N \frac{n^2 A_n^2}{A_1^2} + \frac{E_{ts} + E_{1-2}}{E_{med1,1}} \right) \quad [5]$$

and

$$g(\bar{\omega}_1) = [Q_1^2 (1 - \bar{\omega}_1^2)^2 + \bar{\omega}_1^2]^{-1/2} \quad [6]$$

where $\bar{\omega}_1 = \omega/\omega_1$ and $g(\bar{\omega}_1)$ is a gain factor predicted by the frequency response far from the sample that is used to eliminate the unknown F_1 . According to Eq. 5, when the amplitude setpoint A_1/A_0 is held constant during a scan, the phase lag ϕ_1 is influenced by (i) the tip-sample dissipation E_{ts} (5), (ii) the higher harmonic content of the first eigenmode (which is relatively small) (6) and (iii) the energy propagation between eigenmodes E_{1-2} . Setting $\omega = \omega_1$ and ignoring E_{1-2} and the higher harmonic content (A_n , $n \geq 2$), we recover the classical single harmonic approximation (5). Ignoring E_{1-2} alone, we recover the higher harmonic correction (6). The critical question becomes How large is E_{1-2} as compared with E_{ts} ?

The energy losses per drive cycle E_{ts} and E_{1-2} can be expressed in terms of work integrals as

$$E_{ts} = - \int_0^T F_{ts} \dot{d} dt \quad [7]$$

and

$$E_{1-2} = \int_0^T F_{ts} \dot{q}_2 dt, \quad [8]$$

respectively. Eqs. 7 and 8 are numerically integrated in the simulations of the stiff cantilever C1 in air and the soft cantilever C2 in liquid, both tapping on the dissipative sample ($E_s = 100$ MPa, $\eta_s = 10$ Pa·s) in Fig. 1D and E_s , respectively. In air, the E_{1-2} is ~ 3 orders of magnitude smaller than E_{ts} , and the conventional theory (2, 4, 5) relating phase contrast to tip-sample dissipation holds. In the liquid simulation, however, we have the opposite scenario: E_{1-2} is nearly an order of magnitude greater than E_{ts} and therefore becomes the primary source of phase contrast.

To demonstrate the implications of the energy loss E_{1-2} on phase-contrast imaging in liquids, we compare simulations of phase lag for the stiff cantilever C1 in air and the soft cantilever C2 in liquid tapping on a heterogeneous sample consisting of 3 distinct regions (Fig. 2A): Region I ($E_s = 100$ MPa, $\eta_s = 10$ Pa·s), Region II ($E_s = 100$ MPa, $\eta_s = 0$), and Region III ($E_s = 1$ GPa, $\eta_s = 0$). The simulations in air (Fig. 2B) agree with the conventional theory

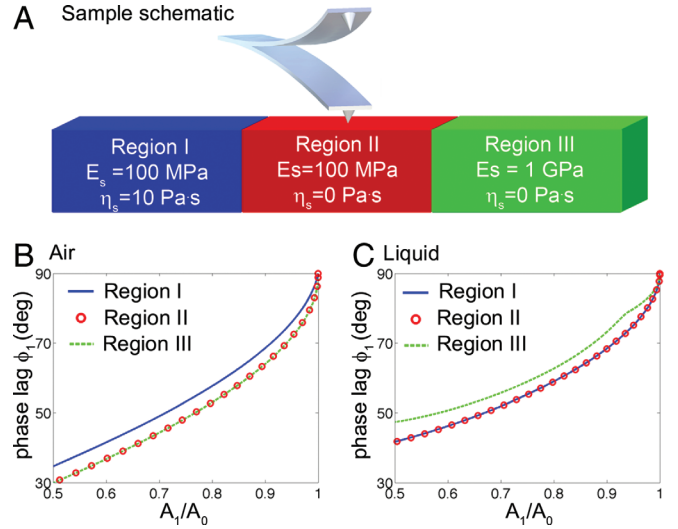


Fig. 2. Simulations of phase lag ϕ_1 vs. amplitude ratio A_1/A_0 for $A_0 = 10$ nm tapping on a hypothetical heterogeneous sample. (A) Schematic of the heterogeneous sample. (B) For a stiff cantilever C1 in air, phase contrasts $\Delta\phi_1^{I-II} > 0$ and $\Delta\phi_1^{I-III} = 0$. (C) For a soft cantilever C2 in liquid, $\Delta\phi_1^{I-II} < 0$ and $\Delta\phi_1^{I-III} = 0$.

(2–5, 7, 26) that the purely elastic regions (II, III) exhibit no phase contrast (26), and the dissipative region (I) has a greater phase lag, resulting in a positive phase contrast $\Delta\phi_1^{I-II} = \phi_1^I - \phi_1^{II} > 0$ (3, 7). However, for the simulations of the soft cantilever C2 in liquid (Fig. 2C), the phase contrast $\Delta\phi_1^{I-II}$ is essentially zero and the phase contrast $\Delta\phi_1^{I-III} < 0$. Thus, when this sample is imaged in air with the stiff cantilever C1, Region I will appear brightest in the phase-lag image. However, Region III will appear brightest in the phase-lag image in liquid.

The difference in phase contrast $\Delta\phi_1^{I-III}$ shown in Fig. 2 indicates that the primary sources of phase contrast are different in the simulations in air and liquid. In air, phase contrast derives from tip-sample dissipation E_{ts} , whereas in liquids, E_{1-2} is the primary source of phase contrast. Although more viscous samples allow greater tip-sample dissipation, stiffer samples increase the momentary excitation of the second eigenmode (24), thus increasing the energy propagation E_{1-2} . More precisely, it is the dominant short-range interaction between the tip and the sample (typically the elastic interactions) that governs the momentary excitation of the second eigenmode and hence the phase contrast.

From Eq. 8, it is clear that the energy propagation E_{1-2} can also be influenced by nonconservative tip-sample interaction forces. However, the viscoelastic contact forces described in Eq. 3, provide a poor mechanism for energy propagation E_{1-2} . We demonstrate this concept in Fig. 3, where the E_s - η_s parameter space for the viscoelastic contact modeled by Eqs. 2 and 3 with the soft cantilever C2 in liquid is shown. Simulations of the oscillating cantilever approaching the sample for both $A_0 = 10$ nm and $A_0 = 1$ nm are performed for a 20×20 grid of points equispaced in log scale for $E_s = [10 \text{ MPa}, 10 \text{ GPa}]$ and $\eta_s = [10 \text{ mPa}\cdot\text{s}, 100 \text{ Pa}\cdot\text{s}]$. The phase-lag surface $\phi_1(E_s, \eta_s)$ is constructed by collecting points on the phase-lag curves where $A_1/A_0 = 0.95$ in each simulation. Fig. 3 demonstrates 3 important results. First, unless the sample is extremely soft and extremely viscous (in the neighborhood of $E_s = 10$ MPa, $\eta_s = 100$ Pa·s; see Fig. 3), phase lag is invariant to changes in viscosity. Second, for moderate- to low-viscosity samples, we find that phase lag ϕ_1 is monotonically increasing with respect to sample elasticity. Third, the trends in phase lag are quite robust—the phase lag simulated for an amplitude $A_0 = 10$ nm (Fig. 3A) is almost identical to the simulations for $A_0 = 1$ nm (Fig. 3B).

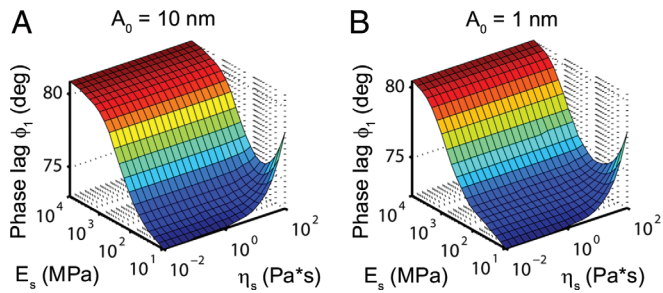


Fig. 3. Simulated phase lag ϕ_1 vs. elastic modulus E_s and viscosity η_s for the soft cantilever C2 in liquid ($A_1/A_0 = 0.95$, $\omega = \omega_1$) for (A) $A_0 = 10$ nm and (B) $A_0 = 1$ nm. In both cases, the phase lag ϕ_1 is invariant with respect to viscosity except in the combination of extremely low elasticity and high viscosity. For moderate to low viscosities, ϕ_1 is monotonically increasing with respect to E_s .

Results and Discussion

The present theory demonstrates that phase contrast for soft cantilevers in liquids can usually be attributed to energy propagation between eigenmodes, which is often mediated by conservative short-range interactions, rather than tip-sample dissipation. When elastic contact forces provide the dominant short-range interaction with the sample, phase contrast then maps the local elastic stiffness. Experimentally, we can determine the primary source of phase contrast based on the following argument. Because both energy losses, E_{1s} (dissipation) and E_{1-2} (propagation), increase the phase lag, we can identify which is the primary energy loss given some prior knowledge of the sample's dissipative properties. For example, when a soft, viscous (dissipative) biological sample is supported on a stiff, nondissipative substrate, then (i) if the soft biological materials have a greater phase lag and appear as a bright region in the phase-lag image in comparison with the stiff substrate (either mica or glass), then tip-sample dissipation is the primary source of phase contrast; or (ii) if the soft biological material should appear as a dark region in the phase-lag image in comparison with the stiff, nondissipative substrate, then E_{1-2} must be the primary source of phase contrast. Finally, in the experiments there is typically a phase offset due to the electronics and/or excitation mechanism. However, this offset is not important to the interpretation of phase-contrast images. We need only to ensure that the image shows the variations in phase lag and not phase, since these are inverse images of each other.

In the first set of experiments, purple membrane (PM) is deposited on mica and gently imaged in buffer solution (see *Materials and Methods* for details). Fig. 4A was obtained with a soft, uniformly magnetically coated cantilever C1 that was excited magnetically. Dark regions in the phase-lag image correspond to the extracellular (EC) face of PM, confirming that energy propagation between eigenmodes is the primary source of the phase contrast.

Although the present theory considers magnetically excited cantilevers, the general form of the energy balance given in Eq. 4 applies to acoustically (base) excited cantilevers as well. Fig. 4B is obtained with a soft cantilever that is acoustically excited; The rough cytoplasmic (CP) face and smooth EC face can be identified in the topographic image. Again, mica appears bright in the phase-lag image, confirming that energy propagation between eigenmodes is the primary source of phase contrast. Furthermore, although it has been demonstrated in high salt-concentration buffers that the stiffnesses of the CP face and the EC face are indistinguishable by force-distance “jump-mode” imaging methods (18), the difference in stiffnesses between the CP and EC faces is clearly resolved in the phase-lag image. Moreover, the phase-lag image suggests that the CP face is slightly softer than the EC face as expected (18).

Fig. 4C contains high-resolution images of the EC face of PM, revealing the trimer assembly of bacteriorhodopsin (bR) which were obtained with acoustic excitation of the second eigenmode of a soft microcantilever (see *Materials and Methods*). The phase-lag image resolves the difference in stiffness between the bR assembly and surrounding lipids.

A second set of experiments was performed by using an acoustically excited Biolever, also in buffer solution. The topography and phase lag ϕ_1 of a single $\phi 29$ virion with DNA packed inside and supported on a silanized glass substrate are shown in Fig. 5A and 5B, respectively. Fig. 5D shows the solid 3-dimensional cryo-electron microscopy (cryo-EM) reconstructed structure of a $\phi 29$ phage predicted by ref. 27 in blue. The cryo-EM reconstruction is imported into WSxM software (28) where a geometric tip dilation algorithm (29) is used to compute the expected dAFM topographic image accounting for the finite size of the tip. In this case, a tip radius $R = 8$ nm is assumed. Fig. 5 clearly resolves the capsid, collar, and tail knob of the virion.

The phase-lag image (Fig. 5B) clearly shows that the soft virus (stiffness ≈ 0.25 N/m) appears dark compared with the glass ($E_s = 65$ GPa), again confirming that the source of phase contrast is energy propagation between eigenmodes. Interestingly, we find the stiffness of the virion changes along the longitudinal in axis (Fig. 5C) in 3 distinct regions, showing how important features can be discerned from the phase-lag image. The phase-lag image clearly resolves the collar (green arrows), which appears as a bright region relative to the capsid and tail knob. We conclude that the collar is stiffer than the capsid. The tail knob is darkest in the phase-lag image, implying that its stiffness is least among

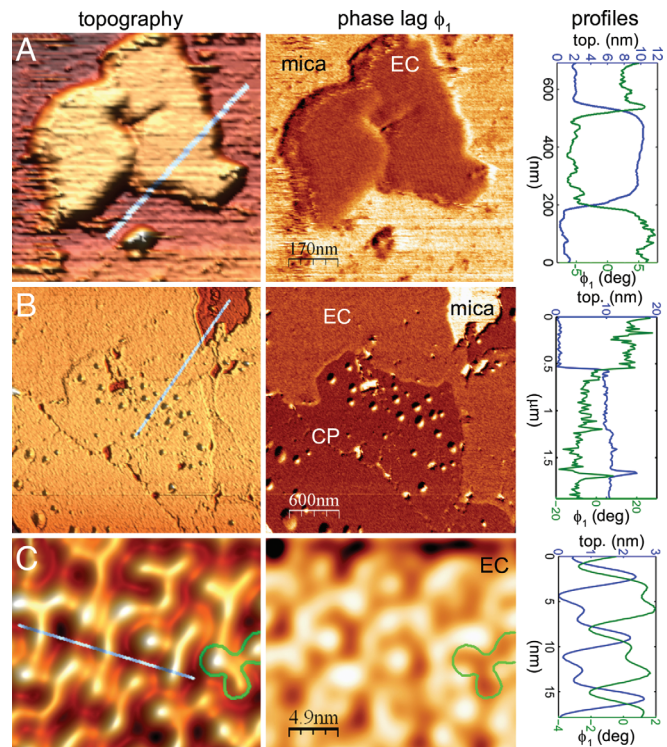


Fig. 4. Purple membrane deposited on mica and imaged in buffer solution. Topography, phase lag, and profile lines of purple membrane (PM) on mica in buffer solution. (A) Rafts of PM (EC face) imaged by magnetic excitation of a soft cantilever C2. (B) Acoustic excitation images of the rough CP face and smooth EC face of PM supported on mica, which are clearly resolved in the phase-lag image. (C) Higher magnification of the EC face from revealing the trimer assembly of bR was obtained with acoustic excitation of the second eigenmode of a soft cantilever. The trimer pattern in the topographic image is reproduced in the phase-lag image. See *Materials and Methods* for more details.

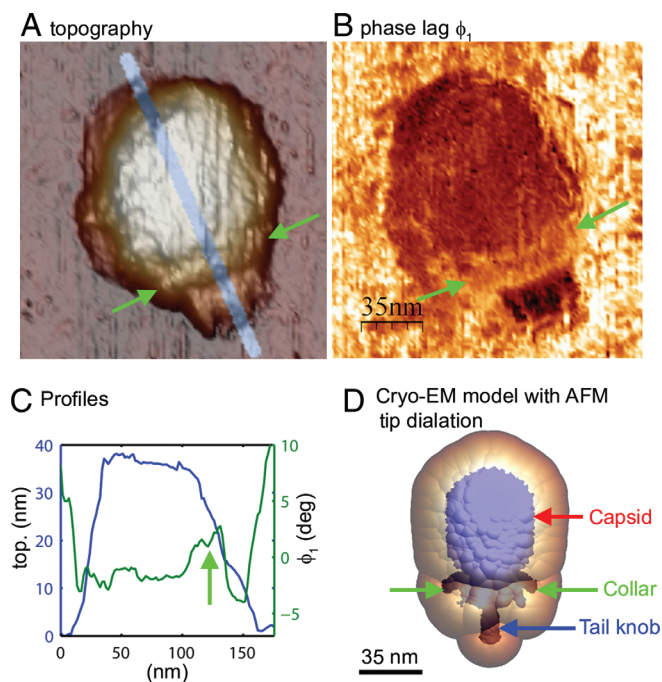


Fig. 5. Experiments on $\phi 29$ virions. (A and B) Topography (A) and phase lag ϕ_1 (B) of a $\phi 29$ phage deposited on a glass substrate and imaged with the Biolever in buffer solution. The phase-lag image reveals a greater phase lag on glass than on the virion supporting the present theory. (C) The profiles for the line shown in A. (D) The 3-dimensional cryo-EM reconstruction of $\phi 29$ (blue) predicted in ref. 27 with a superposed image of the expected AFM topography including geometric tip dialation (29). The structural features of $\phi 29$, such as the collar (green arrows) and the hollow tail knob are clearly resolved in the phase-lag image demonstrating the power phase-lag imaging as a mapping of local elastic stiffness/structural integrity of the virion.

the different parts of the virion, which is expected because it is hollow. It is important to note that differences in local stiffness inferred from the phase-lag image should not be considered as maps of local elastic modulus. The effective stiffness of a nanoscale object encountered by the tip is a combined measure of the elastic modulus and geometry (hollow/solid, curved/flat).

The present theory is also inadvertently supported by prior experimental results using soft cantilevers in liquids. For example, in experiments (30) performed on a patterned surface of hydroxyl- and carboxyl-terminated self-assembled monolayers in 10-mM phosphate buffer, the soft carboxyl region appears dark in the phase-lag image. In experiments (7) performed on PM deposited on a mica substrate in buffer solution (300 mM KCl, 10 mM Tris-HCl), PM appears dark in the phase-lag image. Conventional theory (2, 4, 7, 30) relating phase-lag to tip-sample dissipation predicts the soft, viscous (dissipative) regions will appear brighter in the phase-lag image (greater phase lag) compared with the stiff, non-dissipative regions. However, the dissipative regions of the sample appear darker than the substrate in both experiments (7, 30), confirming the present theory that the energy propagation to higher eigenmodes is the primary source of the phase contrast.

We have shown that phase contrast of soft cantilevers in liquids arises from energy propagation during momentary excitation of higher eigenmodes—a phenomenon that is dictated by short-range interactions with the sample (elastic contact forces, van der Waals, surface hysteresis). Long-range electrostatic double-layer forces can also influence phase contrast if the tip oscillation is comparable to or smaller than the Debye length. However, the theory and experiments described herein consider a commonly encountered situation for dAFM in liquids using soft nonfunctionalized microcantilevers ($k_1 \lesssim 1$ N/m, $Q_1 \lesssim 5$) under

gentle imaging conditions with high salt-concentration buffer solution where the electrostatic DLVO forces are screened (18, 19), and the short-range interactions with the sample are essentially local elastic contact forces. Under these experimental conditions, phase-lag images can be interpreted as a mapping of local sample stiffness. It is only when the sample becomes extremely soft and viscous (see Fig. 3) that tip-sample dissipation plays a role in phase contrast.

Conventional theory that relates phase contrast, a key observable in dAFM, to tip-sample dissipation assumes that the cantilever motion can be described by using a single spatial eigenmode with, perhaps, higher harmonic temporal content. In ambient environments, high quality factors eliminate the energy propagation between eigenmodes, even in the case of bimodal (2-frequency) excitation (31, 32). We have shown that this assumption breaks down when soft cantilevers are used in liquids where the dynamics are naturally multimodal due to the momentary excitation of higher eigenmodes. For soft cantilevers in liquids, this leads to a new energy transfer channel where energy is transferred from the fundamental eigenmode to higher eigenmodes. In stark contrast to the situation in air or vacuum, this result implies that phase contrast of soft microcantilevers in liquids arises due to momentary vibrational energy transfer to the higher eigenmodes rather than tip-sample dissipation. Consequently, under controlled experimental conditions, phase-contrast images can be used to map intricate variations of local sample elasticity of soft biological samples in buffer solutions.

Materials and Methods

Numerical Simulations. All numerical simulations were performed in the open-access, web-based simulation suite VEDA v2.0 (22). Nonsmooth/discontinuous models for tip-sample interaction forces often encountered in dAFM require special treatment in numerical studies (33–35). Accurate and efficient numerical integration of Eq. 1 for nonsmooth/discontinuous interaction models is achieved with the DDASKR routine with a root-finding algorithm based on the DASPK differential algebraic equations software package (36, 37). The key advantage to the DDASKR routine over conventional routines is the ability to solve for the precise location of the sample boundary in state space and proceed to take the appropriate adaptive time steps while the tip is indenting the sample.

Experimental Setups. In the first set of experiments, the extracellular face of wild-type PM was deposited on mica in salt buffer. Wild-type bacteriorhodopsin isolated from *Halobacterium salinarum* strain S9 as PM in the form of lyophilized powder was obtained from Sigma-Aldrich. The PM was deposited on freshly cleaved mica in salt buffer [300 mM KCl, 20 mM Tris-HCl (18)] and imaged by using an Agilent 5500 AFM system. Results are shown in Fig. 4A was obtained with a soft, magnetically coated cantilever C1 that was excited magnetically (38) at $A_0 = 15$ nm ($A_1/A_0 = 0.8$). Fig. 4B was obtained with an Olympus cantilever (OMCL-RC800PB; $k_1 = 0.58$ N/m, $Q_1 = 1.8$, $Q_2 = 3.3$, $\omega_1 = 2\pi \cdot 17$ kHz, $\omega_2 = 7.1\omega_1$) nominal stiffness $k_1 = 0.73$ N/m by using an acoustic excitation at $A_0 = 1.4$ nm ($A_1/A_0 = 0.65$). Fig. 4C was obtained with an Olympus cantilever (OMCL-RC800PB; $k_1 = 0.09$ N/m, $Q_1 = 1.0$, $Q_2 = 3.8$, $\omega_1 = 2\pi \cdot 4.4$ kHz, $\omega_2 = 7.3\omega_1$), nominal stiffness $k_1 = 0.10$ N/m, with an acoustic excitation of the second eigenmode at $A_0 \approx 0.3$ nm ($A_1/A_0 \approx 0.9$). Images were rendered in WSxM software (28). No filters were applied to the images except for those in Fig. 4C, which were filtered using the Mexican hat wavelet filter (39) at a scale of 1.2 nm.

In a second set experiments, a $\phi 29$ virus capsid on a glass substrate was imaged in buffer solution by using an Olympus Biolever (BL-RC150VB; $k_1 = 0.036$ N/m, $Q_1 = 1.2$, $Q_2 = 2$, $\omega_1 = 2\pi \cdot 9.3$ kHz, $\omega_2 = 7.6\omega_1$), nominal stiffness $k_1 = 0.03$ N/m, that was acoustically excited at $A_0 = 9$ nm ($A_1/A_0 = 0.8$). A stock of $\phi 29$ mature virions were imaged with a Nanotec Electrónica S.L in Tris-magnesium-saline buffer (pH 7.8). A single drop of 20 μ L stock solution virions was deposited on silanized glass surface (40), left for 30 minutes, and washed with buffer. The tip was prewetted with 20 μ L of buffer. The nominal $k_1 = 0.03$ N/m Biolever was chosen specifically to prevent damage to the fragile capsids (10). Images were rendered in WSxM software (28).

Stiffnesses of the first eigenmode were calibrated by using Sader's method in air (41). Natural frequencies and quality factors were determined from the thermal (undriven) vibration spectrum in liquid. Excitation frequencies were chosen from the peak of the tuning curve closest to the corresponding peak in the thermal vibration spectrum.

ACKNOWLEDGMENTS. The authors thank Prof. Ron Reifengerger (Purdue University, West Lafayette, IN) for helpful discussions. This research was supported by the National Science Foundation under grant CMMI-0700289 (Dr. Eduardo Misawa is the program manager).

1. Garcia R, Perez R (2002) Dynamic atomic force microscopy methods. *Surf Sci Rep* 47:197–301.
2. Garcia R, Magerle R, Perez R (2007) Nanoscale compositional mapping with gentle forces. *Nat Mater* 6:405–411.
3. Magonov S, Elings V, Whangbo M (1997) Phase imaging and stiffness in tapping-mode atomic force microscopy. *Surf Sci* 375:L385–L391.
4. Cleveland JP, Anczykowski B, Schmid A, Elings V (1998) Energy dissipation in tapping-mode atomic force microscopy. *Appl Phys Lett* 72:2613–2615.
5. Anczykowski B, Gotsmann B, Fuchs H, Cleveland JP, Elings VB (1999) How to measure energy dissipation in dynamic mode atomic force microscopy. *Appl Surf Sci* 140:376–382.
6. Tamayo J (1999) Energy dissipation in tapping-mode scanning force microscopy with low quality factors. *Appl Phys Lett* 75:3569–3571.
7. Stark M, Moller C, Muller DJ, Guckenberger R (2001) From images to interactions: High-resolution phase imaging in tapping-mode atomic force microscopy. *Biophys J* 80:3009–3018.
8. Stark M, Stark RW, Heckl WM, Guckenberger R (2002) Inverting dynamic force microscopy: From signals to time-resolved interaction forces. *Proc Natl Acad Sci USA* 99:8473–8478.
9. Legleiter J, Park M, Cusick B, Kowalewski T (2006) Scanning probe acceleration microscopy (SPAM) in fluids: Mapping mechanical properties of surfaces at the nanoscale. *Proc Natl Acad Sci USA* 103:4813–4818.
10. Xu X, Carrasco C, de Pablo PJ, Gomez-Herrero J, Raman A (2008) Unmasking imaging forces on soft biological samples in liquids when using dynamic atomic force microscopy: A case study on viral capsids. *Biophys J* 95:2520–2528.
11. Basak S, Raman (2007) A Dynamics of tapping mode atomic force microscopy in liquids: Theory and experiments. *Appl Phys Lett* 91:064107.
12. Melcher J, Hu S, Raman (2007) A Equivalent point-mass models of continuous atomic force microscope probes. *Appl Phys Lett* 91:053101.
13. Dankowicz H and Paul MR (2009) Discontinuity-induced bifurcations in systems with hysteretic force interactions. *Proceedings of the 9th Biennial ASME Conference Engineering Systems Design and Analysis* (American Soc of Mechanical Engineers; New York), pp 633–641.
14. Butt HJ, Cappella B, Kappl M (2005) Force measurements with the atomic force microscope: Technique, interpretation and applications. *Surf Sci Rep* 59:1–152.
15. Garcia R, et al. (2006) Identification of nanoscale dissipation processes by dynamic atomic force microscopy. *Phys Rev Lett* 97:016103.
16. Baumgartner W, et al. (2000) Cadherin interaction probed by atomic force microscopy. *Proc Natl Acad Sci USA* 97:4005–4010.
17. Johnson K, Kendall K, Roberts (1971) A Surface energy and contact of elastic solids. *Proc R Soc London Ser A* 324:301.
18. Voitchovsky K, Contera S, Kamihira M, Watts A, Ryan J (2006) Differential stiffness and lipid mobility in the leaflets of purple membranes. *Biophys J* 90:2075–2085.
19. Muller DJ, Engel A (2007) Atomic force microscopy and spectroscopy of native membrane proteins. *Nat Protocols* 2:2191–2197.
20. Hertz H, Reine J (1882) On the contact of elastic solids. *Angew Math* 92:156.
21. Chadwick RS (2002) Axisymmetric indentation of a thin incompressible elastic layer. *SIAM J Appl Math* 62:1520–1530.
22. Melcher J, Kiracofe D, Johnson SD and Raman A (2009) VEDA 2.0 (Virtual Environment for dynamic AFM), 10254/nanohub-r5349.4.
23. Cherry RJ (1979) Rotation and lateral diffusion of membrane-proteins. *Biochim Biophys Acta* 559:289–327.
24. Xu X, Melcher J, Basak S, Reifengerger R, Raman (2008) A compositional contrast of biological materials in liquids using momentary excitation of higher eigenmodes in dynamic atomic force microscopy. *Phys Rev Lett* 102:060801.
25. Sahin O, Quate CF, Solgaard O, Atalar (2004) A resonant harmonic response in tapping-mode atomic force microscopy. *Phys Rev B* 69:165416.
26. Tamayo J, Garcia R (1998) Relationship between phase shift and energy dissipation in tapping-mode scanning force microscopy. *Appl Phys Lett* 73:2926–2928.
27. Tang J, et al. (2008) DNA poised for release in bacteriophage phi 29. *Structure* 16:935–943.
28. Horcas I, et al. (2007) WSxM: A software for scanning probe microscopy and a tool for nanotechnology. *Rev Sci Instrum* 78:013705.
29. Villarrubia JS (1997) Algorithms for scanned probe microscope image simulation, surface reconstruction, and tip estimation. *J Res Natl Inst Stand Technol* 102:425–454.
30. Ashby P, Lieber C (2005) Ultra-sensitive imaging and interfacial analysis of patterned hydrophilic sam surfaces using energy dissipation chemical force microscopy. *J Am Chem Soc* 127:6814–6818.
31. Lozano JR, Garcia R (2008) Theory of multifrequency atomic force microscopy. *Phys Rev Lett* 100:076102.
32. Lozano JR, Garcia R (2009) Theory of phase spectroscopy in bimodal atomic force microscopy. *Phys Rev B* 79:014110.
33. Melcher J, Hu S, Raman (2008) A invited article: VEDA: A web-based virtual environment for dynamic atomic force microscopy. *Rev Sci Instrum* 79:061301.
34. Stark RW (2009) Dynamics of repulsive dual-frequency atomic force microscopy. *Appl Phys Lett* 94:063109.
35. Shampine LF, Reichelt MW (1997) The MATLAB ODE suite. *SIAM J Sci Compu* 18:1–22.
36. Brown PN, Hindmarsh AC, Petzold LR (1994) Using Krylov methods in the solution of large-scale differential-algebraic systems. *SIAM J Sci Compu* 15:1467–1488.
37. VanKeken PE, Yuen DA, Petzold LR (1995) DASP: A new high order and adaptive time-integration technique with applications to mantle convection with strongly temperature- and pressure-dependent rheology. *Geophys Astro Fluid* 80:57–74.
38. Han WH, Lindsay SM, Jing TW (1996) A magnetically driven oscillating probe microscope for operation in liquids. *Appl Phys Lett* 69:4111–4113.
39. Gackenheimer C, Cayon L, Reifengerger R (2006) Analysis of scanning probe microscope images using wavelets. *Ultramicroscopy* 106:389–397.
40. Carrasco C, et al. (2006) DNA-mediated anisotropic mechanical reinforcement of a virus. *Proc Natl Acad Sci USA* 103:13706–13711.
41. Sader JE, Larson I, Mulvaney P, White LR (1995) Method for the calibration of atomic-force microscope cantilevers. *Rev Sci Instrum* 66:3789–3798.